In-situ TEM studies of nanostructured thermoelectric materials: An application to Mg-doped Zn4Sb3 alloy

Ngo, Duc-The; Le, Hung Thanh; Ngo, Nong Van

Published in:
ChemPhysChem

Link to article, DOI:
10.1002/cphc.201700930

Publication date:
2018

Document Version
Peer reviewed version

A EUROPEAN JOURNAL

CHEMPHYSCHEM

OF CHEMICAL PHYSICS AND PHYSICAL CHEMISTRY

Accepted Article

Title: In-situ TEM studies of nanostructured thermoelectric materials: An application to Mg-doped Zn4Sb3 alloy

Authors: Duc-The Ngo, Hung Thanh Le, and Nong Van Ngo

To be cited as: *ChemPhysChem* 10.1002/cphc.201700930

Link to VoR: http://dx.doi.org/10.1002/cphc.201700930

A Journal of

ChemPubSoc Europe

WILEY-VCH

www.chemphyschem.org

10.1002/cphc.201700930

In-situ TEM studies of nanostructured thermoelectric materials: An application to Mg-doped Zn_4Sb_3 alloy

Duc-The Ngo[a,*], Le Thanh Hung[b], and Ngo Van Nong[b,]**

[a] Electron Microscopy Centre, School of Materials, University of Manchester, Oxford Road, Manchester M13 9PL, United Kingdom

[b] Department of Energy Conversion and Storage, Technical University of Denmark, DTU-Risø Campus, 4000 Roskilde, Denmark

Corresponding authors:

* duc-the.ngo@manchester.ac.uk

** ngno@dtu.dk

Abstract

We demonstrate an advanced approach using advanced *in-situ* transmission electron microscopy (TEM) to understand the interplay between nanostructures and thermoelectric (TE) properties of high-performance Mg-doped Zn_4Sb_3 TE system. With the technique, microstructure and crystal evolutions of TE material have been dynamically captured as a function of temperature from 300 K to 573 K. On heating, we have observed clearly precipitation and growth of a Zn-rich secondary phase as nanoinclusions in the matrix of primary Zn_4Sb_3 phase. Elemental mapping by STEM-EDX spectroscopy reveals enrichment of Zn in the secondary Zn_6Sb_5 nanoinclusions during the thermal processing without decomposition observed. Such nanostructure strongly enhances the phonon scattering resulting in the decrease in the thermal conductivity leading to a *zT* value of 1.4 at 718 K.

Keywords: thermoelectrics, transmission electron microscopy, energy dispersive X-ray spectroscopy, high angle annular dark field, selected area electron diffraction, Zn-Sb compounds.

1. Introduction

High-performance thermoelectric (TE) materials are usually heavily doped semiconductors to get a high electrical conductivity (σ). With expectation of low thermal conductivity, various phonon scattering processes allow reducing the thermal conductivity (κ). The combination of these factors leads to high TE figures of merit, $zT = S^2\sigma T/\kappa$ (where S is the Seebeck coefficient and T is the temperature,). Creating nanostructures in TE materials is one of the promising approaches to obtain high zT:[1] (i) enhancing the density of state near Fermi level via quantum confinement and as a result increases the thermopower to decouple thermopower and electrical conductivity; (ii) reducing the thermal conductivity by introducing more phonon scattering on the nanostructures while preserving carrier mobility and electronic conduction. In most nanostructured TE materials, understanding the interplay between nanostructures and TE properties under dynamic conditions plays an important role to develop high performance and stable TE materials and devices.[2]

The idea of nanostructured thermoelectric materials was firstly reviewed by Dresselhaus et al.,[3] in which low-dimensional thermoelectricity was believed to start with the introduction of two strategies: the use of quantum-confinement phenomena to enhance and control S but σ independently, and controlling of the thermal conductivity by the use of numerous interfaces to scatter phonons more effectively than electrons, and to scatter preferentially those phonons.[4] Among these strategies, nanocomposite TE materials, which are designed to introduce nanometer-sized polycrystallines and interfaces into bulk materials, can be considered as an effective approach to produce high-performance TE materials with low cost and large volume.[5] It is realised by the formation of nanometer-sized (grain size ~5 nm–10 μm, typically) grains on a main matrix that creates extensive interfaces between the neighbouring nanoparticles, which allows significantly lowering the thermal conductivity.[5] Nanocomposites with enhanced zT have been found in the various TE material families,

including Bi_2Te_3-based nanocomposites,[6–9] PbTe-based nanostructured materials,[10–12] SiGe-based nanocomposites,[13–16] and ZnSb alloy,[17–21] etc.

Zn_4Sb_3 alloy has been well-known as high-performance TE materials in the intermediate temperature range (473−673 K). In addition, Zn_4Sb_3 consists of low-cost and abundant elements, hence, it has been considered as one of the best candidate p-type for making a low cost and high conversion efficiency thermoelectric power generator (TEG).[22–28] Despite those advantages, thermal instability of Zn_4Sb_3 is the main factor responsible for limiting its practical application in TEG.[18,29–35] Therefore, many studies have focused on the stability of Zn_4Sb_3 in different conditions *e.g.* inert gas,[34–36] air,[36] static vacuum,[34] and dynamic vacuum.[34,37] In those works, various techniques *e.g.* thermogravimetric analyses (TGA),[34,35] high-temperature powder X-ray,[37] or high-temperature synchrotron powder X-ray diffraction,[18,29–33] were employed to understand the degradation rate of materials. Additionally, a theoretical model was also used to calculate time−temperature−transformation of Zn_4Sb_3 phase.[38] It was shown that under heating condition Zn_4Sb_3 started degrading below 500 K in air,[36] and higher 543 K dynamic vacuum,[34,37] however stable under Argon gas and static vacuum up to 670 K.[34,35] All reports focused on decomposition of Zn_4Sb_3 proposed migration of high dynamic Zn into Zn interstitial (hcp) sites at elevated temperature as the main mechanism of Zn_4Sb_3 degradation.[18,29–38] The decomposition of Zn_4Sb_3 was also proposed to suppress into ZnSb and Zn[38–41], and this hypothesis was only supported by indirect experimental work *e.g.* TE characterization in different conditions and high-temperature powder X-ray diffraction,[18,34] which could only give very limited understanding the processes at the atomic scales. These remained a number of limitations: (i) the explanation relied on experimental result collected from different type of studied sample i.e. powder materials for XRD and pressed pellet for TE characterization; (ii) the test condition of Zn_4Sb_3 materials was not equivalent to the TE

conditions (*i.e.* thermal cycling, thermal gradient, temperature variation) where the microstructure and crystal evolution could easily occur. So far, no direct experiment has been conducted to prove evidently the hypothesis of material decomposition. Notably, this is likely one of the general issues in most nanostructured TE materials that needs to be clarified using advanced *in-situ* experiments.

In particular, improving thermal stability for Zn_4Sb_3 materials could bring benefit for practical application. Thus, many efforts have been made including element substituting/doping into Zn site including Cd doping,[42] Mg doping,[30] Bi doping,[43] Gd doping,[44] or thermal processing in inert gas (e.g. *Ar*),[45] or melt-spun preparation,[46] or compositing Zn_4Sb_3 with nanostructures,[47] etc. Among them, Mg doping demonstrated an effective improvement on thermal stability by significantly reducing the fraction of decomposition at high temperature (13% compared to 42% in undoped samples).[30] This could be presumably resulted from a unknown structural behavior which was not clearly understood previously.[30,48]

In this study, we propose a useful tool using *in-situ* high-resolution transmission electron microscopy (TEM) combined with high quality compositional analysis to provide deep understanding the TE properties of nanostructured materials and low-cost high-performance Mg-doped Zn_4Sb_3 system was chosen as a typical case study. The crystal and microstructure evolutions of Mg-doped Zn_4Sb_3as a function of temperature from 300 K to 573 K are captured. The TE properties of pressed pellet are also characterized as a function of temperature, and the obtained results will be incorporated with the *in-situ* analyses to explain the origin of high performance as well as the thermal stability of Zn_4Sb_3 materials.

2. Experimental procedures

Ingot alloy with a nominal stoichiometry of $Mg_{0.04}Zn_{3.96}Sb_3$ was prepared from mixture of component elements (99.99% Zn granules, 99.5% Sb powder and 99.5% Mg ingots) sealed in a 10^{-4} Pa quartz ampoule which was then heated to 973 K (700^{o}C) (heating rate 400K/h) in a tube furnace. The ampoule was held horizontally in the furnace at the temperature for 2 h under continuous rotation to ensure homogeneous melting before quenching into ice water. Details of preparation and processing can be referred to previous work published elsewhere.[30]

Crystallography and microstructure of the materials were studied using transmission electron microscopy (TEM) under both *in-situ* and *ex-situ* heating experiments in a Jeol JEM 3000F and a FEI Tecnai F30 which are both equipped with field emission gun (FEG), high angle annular dark-field (HAADF) detector and silicon drift detector (SSD) for energy dispersive X-ray (EDX) spectroscopy. TEM specimens were prepared by mechanical grinding and then final thinning using Ar ion milling. *In-situ* heating experiment inside TEM chamber of the Jeol 3000F TEM was performed on a Gatan heating holder with a Ta cup (Model No.628Ta)[49] *Ex-situ* EDX analysis was conducted using the FEI Tecnai F30 with a low background holder specifically used for EDX spectroscopy analysis.

Measurements of the Seebeck coefficient and the electrical resistivity were simultaneously conducted using a commercial equipment Ulvac-Riko Zem-3 from room temperature up to 718 K under helium pressure of 0.1 Bar. The thermal conductivity (κ) was calculated from the measured thermal diffusivity (γ), the mass density (δ), and the specific heat capacity (C_p) using the relation $\kappa = \gamma \times D \times C_p$ in which the thermal diffusivity was measured by laser flash method (Netzsch LFA-457, Germany), the mass density of the sample was obtained by Archimedes' method using water with surfactant, and the specific heat capacity was measured by differential thermal analysis technique using a differential scanning calorimeter

(Netzsch DSC 404C, Germany). The heating rate was about 1K/min for both measurements in ZEM3 and LFA-457 systems.

3. Results and discussion

In-situ heating experiment was performed on the Jeol JEM 3000F TEM using a Gatan heating holder.[50] The experiment was initialized by an imaging process at room temperature (RT), then heating slowly to certain temperatures (about 0.1 K/s), and keeping the specimen at such steady temperatures in 5 minutes for imaging. Temperature on the heating stage was carefully calibrated to be accurate within 3 K. Fig. 1 illustrates microstructural evolution of the studied material under *in-situ* heating experiment combined with TEM imaging.

A well-defined granular structure is observed at room temperature (Fig. 1a) which is later known as primary phase. It is clearly seen that under heating process, the grain structure of the primary phase remains unchanged (Fig. 1b-d). Significant change observed here is the formation of dark-contrast nanoparticles in the grains of the primary phase on heating. Both size and concentration of such nanoparticles tend to increase with increasing the heating temperature. Namely, the nanoparticles likely start to nucleate at about 373 K (Fig. 1b) with average size of 12 nm and increase their average size to 32 nm as heated to 573 K. This growth process could be further visualized using some magnified BF-TEM images (Fig. 2) where the dark-contrast nanoparticles are zoomed in and clearly indicated. In fact, the picture of formation of the nanoparticle in a number of heat-treated TE materials was previously reported in a number of works in which the nanoparticles was commonly referred as nanoinclusions.[18,20,51] Notably, such a nice picture of nanoinclusions formation is directly observed in our work under an *in-situ* experiment where no nanoinclusion exists from the pristine material at room temperature.

To clarify how this evolution affects the crystal structure of the material, selected area electron diffraction (SAD) was also recorded. Fig. 3 shows SAD patterns of the studied material recorded at various temperatures during the heating experiment from which the structural evolution could be understood. As seen from Fig. 3(a), a pattern of diffraction spot is visible when the sample is at room temperature showing single crystalline nature in the area of diffraction where the beam goes through a high-order Laue zone axis. Carefully indexing the pattern (see supplementary information S1) shows a purely single phase structure with a rhombohedral unit cell ($a = b$ = 1.230 nm, c = 1.248 nm) where the electron beam goes through [350] zone axis of the crystal. This spot pattern still exists in the sample under heating process (Fig. 3b,c) indicates that crystal structure of the initial phase is stable on heating. According to previous studies,[37] such a crystal structure could be identical to $Zn_{5.54}Sb_5$ (space group $R\bar{3}c$) with over 99% consistency. Stable spot pattern existing under heating experiment confirms preservation not only of grain structure but also of crystal structure of the primary phase.

Interestingly, the formation of the nanoinclusions in the primary phase matrix on heating (Fig. 1b-d) results in a pattern of diffraction rings (Fig. 3b-c). More rings appear when the temperature increase (Fig. 3c), and the rings pattern becomes sharper and well defined when the structure of the nanoinclusions becomes stable i.e. at temperatures above 573 K. This indicates crystalline structure in the dark nanoinclusions. Indexing the ring pattern using CrysTBox package (Supplementary information, S1, S2)[52] shows another single phase with a trigonal/hexagonal unit cell (a = 1.235 nm, b = 0.775 nm, c = 1.251 nm) which is close to that of Zn_6Sb_5 phase.[37,53] This reveals the formation of two-phase structure (primary rhombohedral $Zn_{5.54}Sb_5$ phase and secondary trigonal Zn_6Sb_5 phase) during heating. Further to structural determination using SAD, crystal structure of the primary and secondary phases are also clarified using convergent beam electron diffraction (CBED), and the results are

represented in Fig. 3d-f. In this case, the microscope was carefully aligned into microprobe scanning mode, and a HAADF image was firstly taken (Fig. 3d) showing typical secondary-phase nanoinclusions (dark areas) grown on matrix of the primary phase (bright area). Subsequently, the electron probe was manipulated to focus onto the regions of secondary-phase nanoinclusions (labeled by (1) in Fig. 3d) and primary phase (labeled by (2) in Fig. 3d) so that the CBED disk patterns were collected using CCD camera. CBED patterns of the primary phase (Fig. 3e) and secondary nanoinclusion phase (Fig. 3f) are precisely confirmed their crystal structure which is well consistent with the data obtained from the SAD above (Details of indexing CBED patterns could be referred to supplementary information, S3).

Formation and growth of the secondary trigonal/hexagonal phase in the matrix of primary of Zn_6Sb_5 phase could be ascribed to the movement and/or self-diffusion of Zn interstitial from the non-stoichiometric counterpart in the material.[54,55] Our observation points out that there is no decomposition process occurred at temperatures below 673 K as suggested by a number of previous studiess.[38,39,53]Origin of the movement and self-diffusion is due to high mobility of Zn atoms which has been known as a high superionic conductor.[56] High-resolution transmission electron microscopy (HRTEM) presented in Fig. 4 allows us to understand deeper into crystalline nature of the primary and secondary phases where the secondary Zn_6Sb_5 phase is visible as nanoprecipitations on the matrix of the primary $Zn_{5.54}Sb_5$ phase. This can be clearly seen via a series of Moiré fringes pattern in the HRTEM image.[57] Such a Moiré pattern is caused by overlap of two precipitated crystal system of which one is the secondary Zn_6Sb_5 nanocrystals. HRTEM image also allows the crystal unit cell of the secondary Zn_6Sb_5 phase to be simulated (Supplementary information, S2). It is notably interesting to note that such an evolution of two-phase structure could only be observed in TEM as a superior characterization technique, and *in-situ* TEM particularly helps to understand the structural evolution in atomic-level scale.

In supplement to new picture of structural evolution in our studied Mg-doped Zn_4Sb_3 material, compositional analysis would help to view deeper into chemistry of the secondary phase. To realize this, energy dispersive X-ray spectroscopy (EDX) in scanning mode of transmission electron microscopy (STEM) is exploited of which spectroscopy images (elemental map, elemental line distribution, etc.) are quantitatively reconstructed. Fig. 5 represents STEM high angle annular dark field (HAADF) images of the Mg-doped Zn_4Sb_3 at room temperature and at 573 K where the secondary phase is observed to precipitate apparently on the primary phase as dark-contrast nanoinclusions. The dark-contrast of the secondary nanoprecipitation phase (Figs. 5b,c) indicates a low average atomic number of the nanoprecipitation than that in the matrix in terms of Z-contrast principle in STEM-HAADF image,[51] whereas uniform bright contrast (Fig. 5a) in the sample at room temperature shows a compositionally single-phase. Compositionally single-phase nature of the primary phase in Fig. 5a is also proved via uniform distribution of Mg, Zn and Sb elements in STEM-EDX maps of such elements (supplementary information, S4).

Fig. 6 illustrates STEM-EDX elemental maps and elemental line distribution of the Mg-doped Zn_4Sb_3 sample after heating to 573 K and keeping there for 15 minutes. Distribution maps of Zn and Mg clearly show enrichments of these elements in the precipitated nanoinclusions denoted by enhanced brightness in the area of nanoprecipitation in their elemental maps (Figs. 6b,d). The enrichment results in an average atomic weight lower than the matrix region and as a result causes darker contrast in the STEM-HAADF (Fig. 6a). Oppositely, the variation of Sb concentration from the primary matrix to the secondary nanoprecipitation seems to be so small that it could not be seen in the EDX elemental map as shown in Fig. 6c. Variation of elemental concentrations from primary matrix to the secondary nanoprecipitation could be further seen quantitatively in Fig. 7 where EDX distributions of Zn and Sb along a line in HAADF image (Fig. 7a) are plotted (Fig. 7b). It is obviously seen

that the concentration of Zn relative to Sb increases evidently from the matrix to the nanoprecipitation denoted by the peaks of in the Zn concentration plot (Fig. 7b). The increase of Zn concentration in the nanoprecipitated phase results in a lower average atomic weight of the secondary phase so that it looks darker in the STEM HAADF images as shown in figures 4-7. It is also consistent with elemental map (Fig. 6b,c) where the enhanced brightness visible as enrichments of Mg and Zn. In addition, we also observe a slight increase of Zn concentration in the nanoprecipitation nanodots as increasing the heating temperature.

In fact, decomposition can only be observed when the sample was heated over 673 K. In this scenario, secondary Zn-rich phase grows quickly in both size and density whilst the grain structure of the primary phase shrinks quickly. This evolution results in a decomposition process like a zone melting as proposed by previous authors.[38,39,53] This process also causes damaging to the TEM specimen and prohibits further characterization of decomposed sample. However, such a quick process in a short moment is about enough to prove decomposition of Zn_4Sb_3 at high temperature. It is also supplementary to the story that decomposition is not denoted by formation of secondary nanoprecipitated phase but a consequence of the growth of this phase due to migration of Zn under the heat at high temperature.[54,55] In the Zn_4Sb_3 structure, there are 18 Sb^{3-} and 12 Sb^{2-} ions per unit cell corresponding to total of 78 negative charges. To balance the electric charge, 39 Zn^{2+} are required, but only 36 sites are available. Therefore, three zinc ions need to be filled in the interstitial sites.[25] Migrated Zn atoms at the dislocations could be attributed to the Zn interstitial site due to the fact that they are often very mobile.[58]

All the evidences of structural and compositional evolution from *in-situ* and *ex-situ* experiments suggest a new understanding on the thermal instability of Mg-doped Zn_4Sb_3 below 673 K due to Zn migration rather than a decomposition process. Growth of secondary phase is evidentially illustrated in parallel with enrichment of Zn in the phase in a structurally

stable primary phase. In the temperature range from room temperature to below 673 K, observation evidences unlikely support decomposition process but two-phase structure with growth of Zn-enriched secondary phase by migration of Zn atoms. Decomposition at high temperature range above 673 K is likely demonstrated as a consequence of growth of the secondary phase when the migration become inflation.

Thermoelectric properties of Mg-doped Zn_4Sb_3 are investigated as a function of temperature from 300 K to 718 K as presented in Figure 8. It can be seen that the electrical resistivity has two tendencies i.e. metallic conducting behavior in the temperature range of 300 K to 520 K and semiconducting behavior from 520 K to 718 K, as showed in Fig. 8a. Similarly to the trend of resistivity, the Seebeck coefficient has also linearly increased from 117 μV/K at 300 K to 185 μV/K at 520 K, and then it slightly decreases from 520 K to 718 K. Fig. 8b shows the total, electronic, and lattice thermal conductivities of studied sample in the temperature range of 300 K to 718 K. The total thermal conductivity (κ_{total}) is contributed by two main parts of electronic component (κ_e) and lattice component (κ_L) which can be expressed as, $\kappa_{total} = \kappa_{electronic} + \kappa_{lattice}$. The electronic thermal conductivity can be estimated by using the Wiedemann-Franz realation, $\kappa_{electronic} = L\sigma T$, where L is the Lorenz number. For p-type thermoelectric materials, the Lorenz number can be estimated from $L = 1.5 + exp[-|\alpha|/116]$.[59] It is clearly seen that the lattice thermal conductivity rapidly decreases with increasing temperature, while the electronic component tends to increase as the temperatures increase above 600 K. From the data one can identify that the lattice thermal conductivity is dominated at temperature lower 620 K and from 620 K to 718 K the electronic thermal conductivity is the main contribution to the total thermal conductivity of sample. The rapid decreased lattice thermal conductivity with increasing temperature could be associated with the structural deformation from primary phase to the secondary phase. Such a reduction in the lattice thermal conductivity was predicted and observed in previous studies.[60,61]

From measured Seebeck coefficient, electrical and thermal conductivities the material figure of merit, *zT*, is calculated and plotted in Fig. 8c. As can be seen the *zT* value is increased with increasing temperature and reach a maximum value of 1.4 at 718 K. This value is slightly lower than the non-doped Zn_4Sb_3 sample,[34] however this still among highest *zT* in the medium temperature range. Aforementioned, the high *zT* value has significantly contributed from low thermal and electrical conductivities.

Co-existence of nanoinclusion phase in the matrix phase brings benefit for enhancing the thermoelectric performance. Firstly, due to the size of nano-inclusions (10-40 nm) is smaller than mean phonon wavelength (commonly 40-260 nm), the secondary phase nano-precipitations are believed to affect the thermal conductivity by altering the phonon spectrum itself.[62] In this case, they would scatter phonons in much the same way as point defects in which the phonon scattering relaxation time could be written as a function of the "defect" concentration:[62]

$$\frac{1}{\tau_d} = V_a c_i \left(\frac{m_i - m_{ave}}{m_{ave}} \right)^2 \frac{\omega^4}{4\pi v^3} \qquad (1)$$

Where, m_i is the mass of the defect, c_i is the defect concentration, m_{ave} is the average mass of the atoms in the system, V_a is an atomic volume, and v is the speed of sound, respectively. High density of nano-precipitation secondary phase in the sample results in a reduction of the phonon scattering relaxation, and therefore leading to a significant decreasing in the thermal conductivity to enhance the TE *zT*. Secondly, no grain boundary between the primary and secondary phases is observed in the sample that would remain good electrical conductivity because of no electronic scattering on the grain boundaries.[63]

Moreover, an intrinsic structural feature of the studied materials, high density of misfit dislocations (Fig. 4) also gives rise to the thermoelectric performance by enhancing the phonon scattering on the dislocation. Such a phonon scattering can significantly decrease the

phonon relaxation time,[64,65] and as a result, the thermal conductivity as followed the dependence:[62]

$$\frac{1}{\tau_s} = \frac{2^{3/2}}{3^{7/2}} N_d b^2 \gamma^2 \omega \quad (2)$$

Here, N_d is the dislocation density, b is Burgers vector, γ is the Grüneisen parameter, and ω is the phonon frequency, respectively. Misfit dislocations with high density are obviously observed in our studied materials, and they would make an important contribution to reduce the thermal conductivity of the material. Nanoinclusions causes a signification reduction of phonon relaxation time, and therefore, results in a decrease of the thermal conductivity which depends on the relaxation time, $<\tau>$:[17]

$$k_e = \sigma T \frac{k_B^2}{e^2}\left(\frac{\langle \tau.z^2 \rangle}{\langle \tau \rangle} - \left[\frac{\langle \tau.z \rangle}{\langle \tau \rangle}\right]^2\right) \quad (3)$$

With T is the temperature, k_B is the Boltzmann's constant, e is the elementary charge, and σ is the electrical conductivity which is dependent on the relaxation time as a function:[17]

$$\sigma = \frac{e^2}{m_c} \frac{(2 m_d k_B T)^{3/2}}{3\pi^2 \hbar^3} \langle \tau \rangle \quad (4)$$

Where m_c, m_d are effectives masses of conductors and density of states, k_B is Boltzmann constant, e is elementary charge, and $\hbar$ is the Planck constant, respectively.

4. Conclusions and Outlooks

We have demonstrated an effective approach using *in-situ* TEM to study dynamic behavior of thermoelectric nanostructured materials. With this method, a new story of structural and compositional evolution in a Mg-doped Zn_4Sb_3 system was proposed. Thermally stable two-

phase structure composed of primary $Zn_{5.54}Sb_5$ and secondary Zn_6Sb_5 phases was evidentially observed to grow under heating experiments. Enrichment of Zn and Mg elements in the secondary nanoprecipitated phase was quantitatively revealed from heating experiments where the decomposition could only be observed when the heating temperature was above 673 K. It was presumed that this decomposition is likely a consequence of the increasing enrichment of Zn in the secondary nanoprecipitated phase. This new understanding could help to find new routes to enhance thermal stability of Zn_4Sb_3 alloys for practical applications.

Based on the story of dynamic thermal evolution of ZnSb nanostructure as a typical case study, we have proved that *in-situ* electron microscopy including transmission electron microscopy, scanning electron microscopy combined with well-designed *in-situ* experiments would bring breakthrough understanding of materials behavior for both practical applications and fundamental research.

Acknowledgements

We would like to acknowledge Programme Commission on Sustainable Energy and Environment, The Danish Council for Strategic Research for sponsoring our research via the ‘‘CTEC - Center for Thermoelectric Energy Conversion’’ (No. 1305-00002B) projects. We would like to thank TEGnology ApS (Vejle, Denmark) for material producing. Technical support from Mr. Joseph Ward and Ms. Ebtisam Abdellahi for materials processing and specimen preparation are highly acknowledged.

10.1002/cphc.201700930

FIGURES AND TABLES

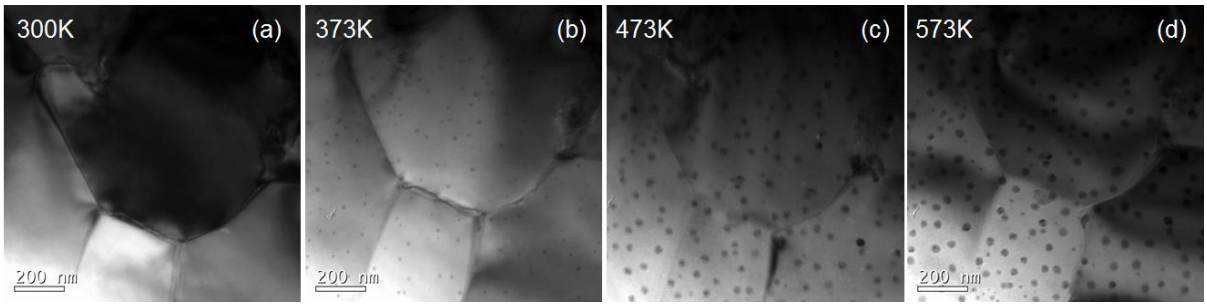

Fig. 1. *In-situ* bright-field TEM (BF-TEM) images of the Mg-doped Zn_4Sb_3 sample as a function of heating temperature from room temperature to 573 K, respectively.

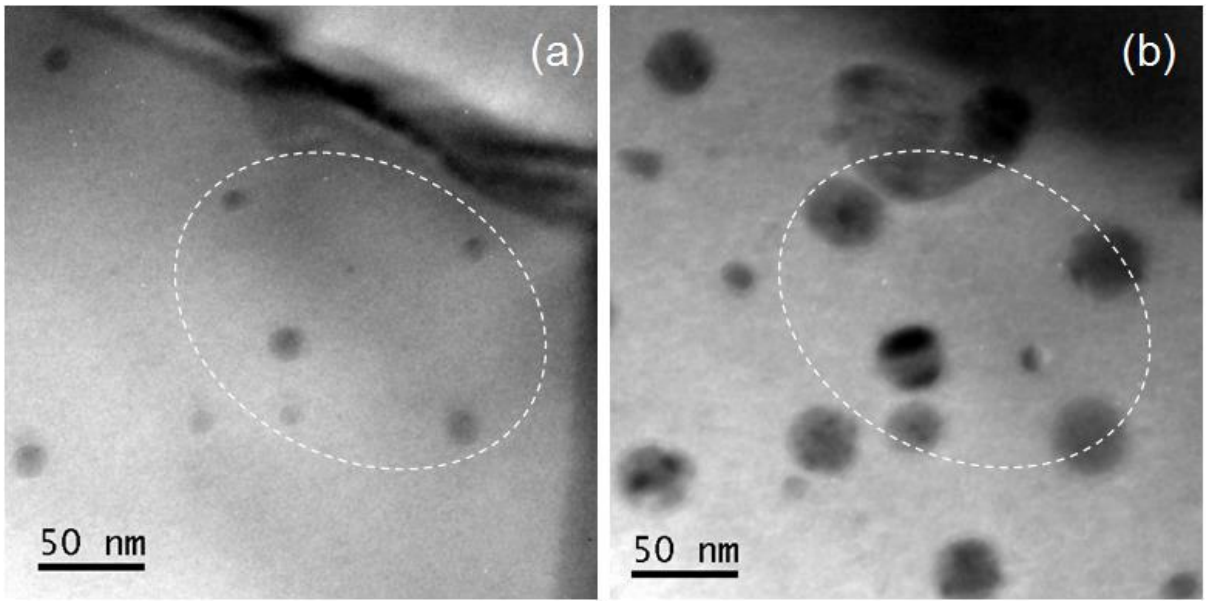

Fig. 2. Magnified BF-TEM images of the studied material at (a) 373K and (b) 573K. The elliptical areas are used to mark and emphasize the growth of the nanoinclusions.

10.1002/cphc.201700930

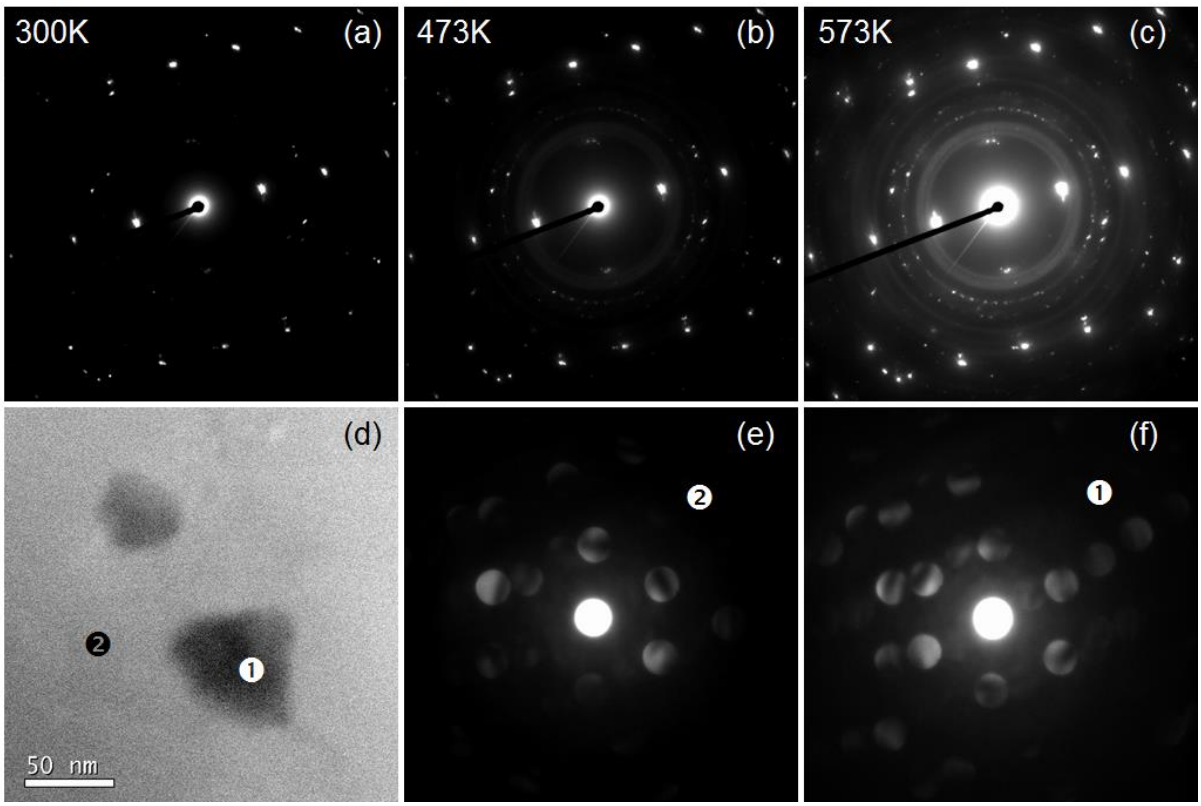

Fig. 3. (a-c) SAD patterns of the studied material recorded at various temperatures during *in-situ* heating experiment: (a) at RT, (b) at 473 K and (c) at 573 K; (d) HAADF image of the studied sample at 573 K, and (e,f) CBED patterns obtained from regions marked on the HAADF image.

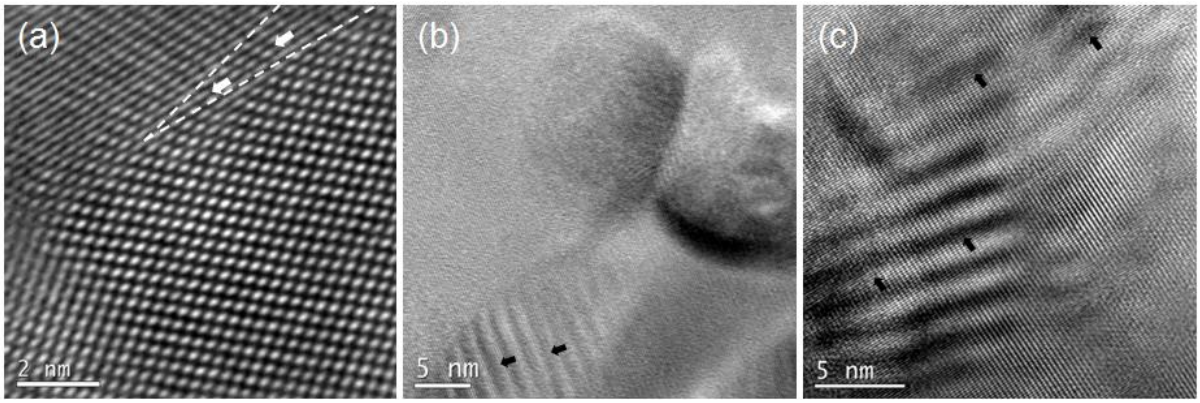

Fig. 4. HRTEM images of (a) primary phase at room temperature with white arrows showing a dislocation, (b,c) two-phase structure at 373 K and 573 K respectively with dark arrows indicating Moiré fringes.

10.1002/cphc.201700930

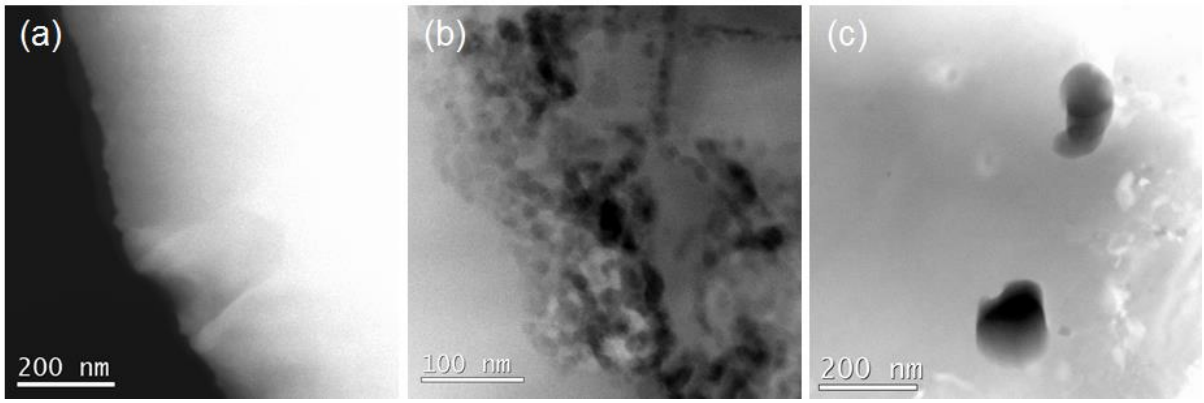

Fig. 5. STEM-HAADF of the Mg-doped Zn_4Sb_3 sample: (a) at room temperature, (b) at 473 K and (c) at 573 K, respectively.

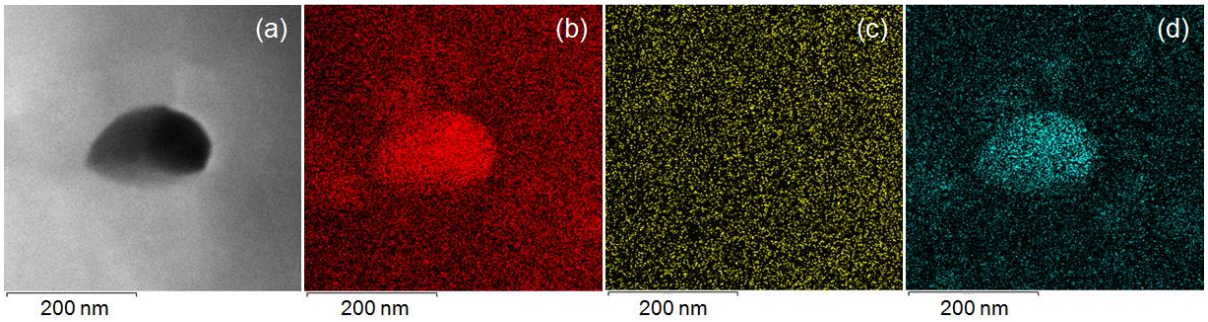

Fig. 6. STEM-EDX of the Mg-doped Zn_4Sb_3 sampled heated to 573 K for 15 minutes: (a) STEM-HAADF image, (b) Zn map, (c) Sb map and (d) Mg map.

10.1002/cphc.201700930

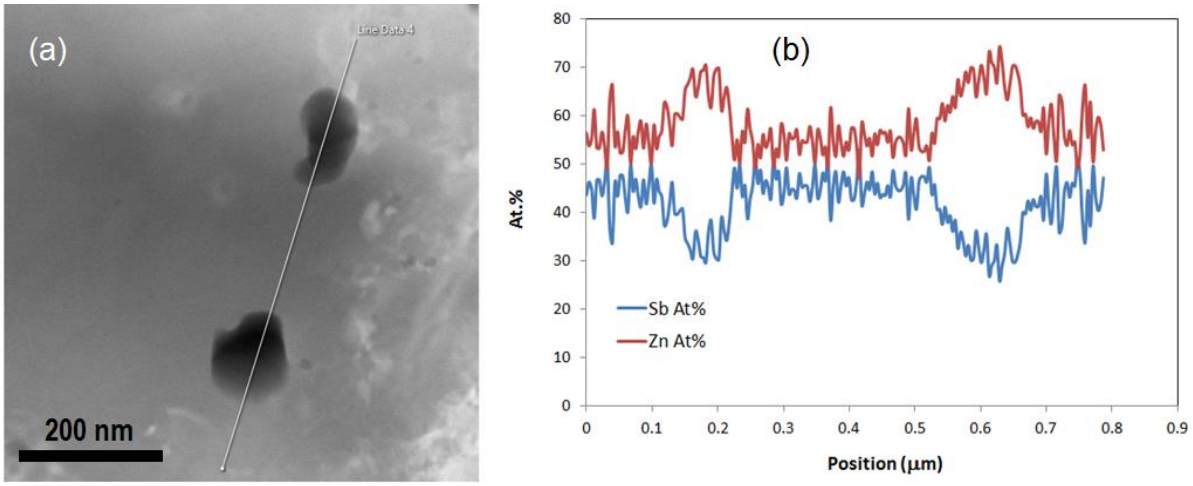

Fig. 7. (a) STEM-HAADF of the Mg-doped Zn_4Sb_3 sample at 573 K showing two typical nanoprecipitated dots, and (b) line profile of Zn and Sb concentration along the white line in (a). The at.% concentration was calculated based on relative Zn and Sb as a 100% sum.

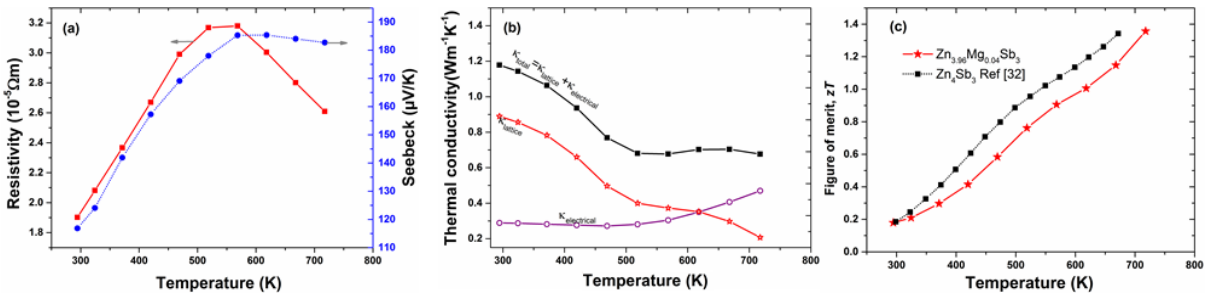

Fig. 8. (a) Electrical resistivity and Seebeck coefficient, (b) thermal conductivity, and (c) figure of merit of Mg-doped Zn_4Sb_3 as a function of temperatures.

References

[1] Z. Chen, G. Han, L. Yang, L. Cheng, J. Zou, *Prog. Nat. Sci. Mater. Int.* **2012**, *22*, 535.

[2] S. Leblanc, *Sustain. Mater. Technol.* **2014**, *1–2*, 26.

[3] M. S. Dresselhaus, G. Chen, M. Y. Tang, R. Yang, H. Lee, D. Wang, Z. Ren, J. P. Fleurial, P. Gogna, *Adv. Mater.* **2007**, *19*, 1043.

[4] K. Koumoto, T. Morimura, *Thermoelectric Nanomaterials*, Springer, **2013**.

[5] Z.-G. Chen, G. Han, L. Yang, L. Cheng, J. Zou, *Prog. Nat. Sci. Mater. Int.* **2012**, *22*, 535.

[6] B. Poudel, Q. Hao, Y. Ma, Y. Lan, A. Minnich, B. Yu, X. Yan, D. Wang, A. Muto, D. Vashaee, X. Chen, J. Liu, M. S. Dresselhaus, G. Chen, Z. Ren, *Science (80-.).* **2008**, *320*, 634.

[7] Y. Lan, B. Poudel, Y. Ma, D. Wang, M. S. Dresselhaus, G. Chen, Z. Ren, *Nano Lett.* **2009**, *9*, 1419.

[8] X. Yan, B. Poudel, Y. Ma, W. S. Liu, G. Joshi, H. Wang, Y. Lan, D. Wang, G. Chen, Z. F. Ren, *Nano Lett.* **2010**, *10*, 3373.

[9] S. N. Zhang, T. J. Zhu, S. H. Yang, C. Yu, X. B. Zhao, *Acta Mater.* **2010**, *58*, 4160.

[10] J. R. Sootsman, H. Kong, C. Uher, J. J. D'Angelo, C.-I. Wu, T. P. Hogan, T. Caillat, M. G. Kanatzidis, *Angew. Chemie Int. Ed.* **2008**, *47*, 8618.

[11] J. He, S. N. Girard, M. G. Kanatzidis, V. P. Dravid, *Adv. Funct. Mater.* **2010**, *20*, 764.

[12] S. Johnsen, J. He, J. Androulakis, V. P. Dravid, I. Todorov, D. Y. Chung, M. G. Kanatzidis, *J. Am. Chem. Soc.* **2011**, *133*, 3460.

[13] R. Basu, S. Bhattacharya, R. Bhatt, M. Roy, S. Ahmad, A. Singh, M. Navaneethan, Y. Hayakawa, D. K. Aswal, S. K. Gupta, *J. Mater. Chem.A* **2014**, *2*, 6922.

[14] J. R. Watling, D. J. Paul, *J. Appl. Phys.* **2011**, *110*, DOI 10.1063/1.3665127.

[15] L. P. Bulat, V. B. Osvenskii, D. A. Pshenay-Severin, *Mater. Today Proc.* **2015**, *2*, 532.

[16] X. W. Wang, H. Lee, Y. C. Lan, G. H. Zhu, G. Joshi, D. Z. Wang, J. Yang, A. J. Muto, M. Y. Tang, J. Klatsky, S. Song, M. S. Dresselhaus, G. Chen, Z. F. Ren, *Appl. Phys. Lett.* **2008**, *93*, 19.

[17] S. V. Faleev, F. Léonard, *Phys. Rev. B* **2008**, *77*, 1.

[18] H. Yin, S. Johnsen, K. A. Borup, K. Kato, M. Takata, B. B. Iversen, *Chem. Commun.* **2013**, *49*, 6540.

[19] D.-B. Xiong, N. L. Okamoto, H. Inui, *Scr. Mater.* **2013**, *69*, 397.

[20] T. Zou, X. Qin, Y. Zhang, X. Li, Z. Zeng, D. Li, J. Zhang, H. Xin, W. Xie, A. Weidenkaff, *Sci. Rep.* **2015**, *5*, 17803.

[21] P. Rauwel, O. M. Laøvvik, E. Rauwel, E. S. Toberer, G. J. Snyder, J. Taftaø, *Phys. Status Solidi A* **2011**, *208*, 1652.

[22] D. Eklof, A. Fischer, Y. Wu, E.-W. Scheidt, W. Scherer, U. Haussermann, *J. Mater. Chem. A* **2013**, *1*, 1407.

[23] A. B. Blichfeld, B. B. Iversen, *J. Mater. Chem. C* **2015**, *3*, 10543.

[24] T. Caillat, J.-P. Fleurial, A. Borshchevsky, *J. Phys. Chem. Sol.* **1997**, *58*, 1119.

[25] G. J. Snyder, M. Christensen, E. Nishibori, T. Caillat, B. B. Iversen, *Nat. Mater.* **2004**, *3*, 458.

[26] G. Zhu, W. Liu, Y. Lan, G. Joshi, H. Wang, G. Chen, Z. Ren, *Nano Energy* **2013**, *2*, 1172.

[27] A. Faghaninia, C. S. Lo, *J. Phys. Condens. Matter* **2015**, *27*, 125502.

[28] X. Yang, J. Lin, G. Qiao, Z. Wang, *Appl. Phys. Lett.* **2015**, *106*, 13904.

[29] B. B. Iversen, *J. Mater. Chem.* **2010**, *20*, 10778.

[30] H. Yin, B. B. Iversen, *Sci. Adv. Mater.* **2011**, *3*, 592.

[31] H. Yin, M. Christensen, B. L. Pedersen, E. Nishibori, S. Aoyagi, B. B. Iversen, *J. Electron. Mater.* **2009**, *39*, 1957.

[32] B. L. Pedersen, H. Yin, H. Birkedal, M. Nygren, B. B. Iversen, *Chem. Mater.* **2010**, *22*, 2375.

[33] S. Y. Wang, X. Y. She, G. Zheng, F. Fu, H. Li, X. F. Tang, *J. Electron. Mater.* **2012**, *41*, 1091.

[34] T. Caillat, J.-P. Fleurial, A. Borshchevsky, *J. Phys. Chem. Solids* **1997**, *58*, 1119.

[35] T. Caillat, J.-P. Fleurial, in *IECEC 96. Proc. 31st Intersoc. Energy Convers. Eng. Conf.*, IEEE, **1996**, pp. 905–909.

[36] H. Yin, B. L. Pedersen, B. B. Iversen, *Eur. J. Inorg. Chem.* **2011**, *2011*, 2733.

[37] Y. Mozharivskyj, A. O. Pecharsky, S. Bud'ko, G. J. Miller, *Chem. Mater.* **2004**, *16*, 1580.

[38] J. Lin, X. Li, G. Qiao, Z. Wang, J. Carrete, Y. Ren, L. Ma, Y. Fei, B. Yang, L. Lei, J. Li, *J. Am. Chem. Soc.* **2014**, *136*, 1497.

[39] A. Wrona, K. Bilewska, J. Mazur, M. Lis, M. Staszewski, *J. Alloys Compd.* **2014**, *616*, 350.

[40] T. Zhang, K. Zhou, X. F. Li, Z. Q. Chen, X. L. Su, X. F. Tang, *J. Mater. Sci.* **2016**, *51*, 2041.

[41] P. Rauwel, O. M. Lovvik, E. Rauwel, E. S. Toberer, G. J. Snyder, J. Tafto, *Phys. Status Solidi A* **2011**, *208*, 1652.

[42] H. Yin, M. Christensen, B. L. Pedersen, E. Nishibori, S. Aoyagi, B. B. Iversen, *J. Electron. Mater.* **2010**, *39*, 1957.

[43] L. Zhou, W. Li, J. Jiang, T. Zhang, Y. Li, G. Xu, P. Cui, *J. Alloys Compd.* **2010**, *503*, 464.

[44] B. Ren, M. Liu, X. Li, X. Qin, D. Li, T. Zou, G. Sun, Y. Li, H. Xin, J. Zhang, *J. Mater. Chem. A* **2015**, *3*, 11768.

[45] H. Yin, B. L. Pedersen, B. B. Iversen, *Eur. J. Inorg. Chem.* **2011**, *2011*, 2733.

[46] D. Qi, X. Tang, H. Li, Y. Yan, Q. Zhang, *J. Electron. Mater.* **2010**, *39*, 1159.

[47] H. Yin, S. Johnsen, K. A. Borup, K. Kato, M. Takata, B. B. Iversen, *Chem. Commun.* **2013**, *49*, 6540.

[48] X. He, Y. Fu, D. J. Singh, L. Zhang, *J. Mater. Chem. C* **2016**.

[49] Y.-J. Chen, B. Zhang, Q.-Q. Ding, Q.-S. Deng, Y. Chen, Z.-T. Song, J.-X. Li, Z. Zhang, X.-D. Han, *J. Alloys Compd.* **2016**, *678*, 185.

[50] Y.-J. Chen, B. Zhang, Q.-Q. Ding, Q.-S. Deng, Y. Chen, Z.-T. Song, J.-X. Li, Z. Zhang, X.-D. Han, *J. Alloys Compd.* **2016**, *678*, 185.

[51] Ø. Prytz, a. E. Gunnæs, O. B. Karlsen, T. H. Breivik, E. S. Toberer, G. Jeffrey Snyder, J. Taftø, *Philos. Mag. Lett.* **2009**, *89*, 362.

[52] M. Klinger, A. Jager, *J. Appl. Crystallogr.* **2015**, *48*, 2012.

[53] P. Rauwel, O. M. La??vvik, E. Rauwel, E. S. Toberer, G. J. Snyder, J. Tafta??, *Phys. Status Solidi Appl. Mater. Sci.* **2011**, *208*, 1652.

[54] O. M. Løvvik, P. Rauwel, Ø. Prytz, *Comput. Mater. Sci.* **2011**, *50*, 2663.

[55] T. Zhang, K. Zhou, X. F. Li, Z. Q. Chen, X. L. Su, X. F. Tang, *J. Mater. Sci.* **2016**, *51*, 2041.

[56] E. S. Toberer, P. Rauwel, S. Gariel, J. Taftø, G. J. Snyder, *J. Mater. Chem.* **2010**, *20*, 9877.

[57] J. He, M. G. Kanatzidis, V. P. Dravid, *Mater. Today* **2013**, *16*, 166.

[58] C. S. Birkel, E. Mugnaioli, T. Gorelik, U. Kolb, M. Panthöfer, W. Tremel, *J. Am. Chem. Soc.* **2010**, *132*, 9881.

[59] H.-S. Kim, Z. M. Gibbs, Y. Tang, H. Wang, G. J. Snyder, *APL Mater.* **2015**, *3*, 41506.

[60] M. Amsler, S. Goedecker, W. G. Zeier, G. J. Snyder, C. Wolverton, L. Chaput, *Chem. Mater.* **2016**, *28*, 2912.

[61] L. T. Zhang, M. Tsutsui, K. Ito, M. Yamaguchi, *J. Alloys Compd.* **2003**, *358*, 252.

[62] A. Chernatynskiy, D. R. Clarke, S. R. Phillpot, in *Handb. Nanosci. Eng. Technol.* (Eds.: W.A.I. Goddard, D. Brenner, S.E. Lyshevski, G.J. Iafrate), CRC Press, **2003**, pp. 545–572.

[63] J.-F. Li, W.-S. Liu, L.-D. Zhao, M. Zhou, *NPG Asia Mater.* **2010**, *2*, 152.

[64] S. N. Girard, J. He, C. Li, S. Moses, G. Wang, C. Uher, V. P. Dravid, M. G. Kanatzidis, *Nano Lett.* **2010**, *10*, 2825.

[65] S. Il Kim, H. A. Mun, H. S. Kim, S. W. Hwang, J. W. Roh, D. J. Yang, W. H. Shin, X. S. Li, Y. H. Lee, G. J. Snyder, S. W. Kim, *Science (80-.).* **2015**, *348*, 109.